Article type: Communication

Spontaneous Formation of Noble- and Heavy-Metal-Free Alloyed Semiconductor Quantum Rods for Efficient Photocatalysis

Dechao Chen, Huayang Zhang, Yunguo Li, Hongqi Sun, Lai-Chang Zhang, Shaobin Wang, Martin Saunders, Emily Barker, Guohua Jia*

D. Chen, E. Barker, Dr. G. Jia
Curtin Institute of Functional Molecules and Interfaces
School of Molecular and Life Sciences, Curtin University
GPO Box U1987, WA 6845, Australia
E-mail: guohua.jia@curtin.edu.au

H. Zhang, Prof. S. Wang
Department of Chemical Engineering and CRC for Contamination Assessment and Remediation of the Environment (CRC CARE)
Curtin University, GPO Box U1987, WA 6845, Australia

Dr. Y. Li
Faculty of Mathematical and Physical Sciences, University College London, Gower Street, London WC1E 6BT, United Kingdom

Prof. H. Sun, Prof. L.C. Zhang,
School of Engineering
Edith Cowan University
270 Joondalup Drive, Joondalup, WA 6027, Australia

Prof. M. Saunders
Centre for Microscopy, Characterization and Analysis (CMCA)
The University of Western Australia
Perth, WA 6009, Australia

Quasi-one-dimensional cadmium chalcogenide quantum rods (QRs) are benchmark semiconductor materials that have been combined with noble metals to constitute QR heterostructures for efficient photocatalysis. However, the high toxicity of cadmium and cost of noble metals are the main obstacles to their widespread use. Herein we report a facile colloidal synthetic approach that leads to the spontaneous formation of cadmium-free alloyed ZnS_xSe_{1-x} QRs from polydisperse ZnSe nanowires by the etching of alkylthiol. The obtained non-noble metal ZnS_xSe_{1-x} QRs can not only be directly adopted as efficient photocatalysts for water oxidation, showing a striking oxygen evolution capability of 3000 µmol g^{-1} h^{-1}, but also be utilized to prepare QRs-sensitized TiO_2 photoanodes which present enhanced photoelectrochemical (PEC) activity. Density functional theoretical (DFT) simulations reveal that alloyed ZnS_xSe_{1-x} QRs have highly active Zn sites on the (100) surface and reduced oxygen evolution energy barrier, which in turn, are beneficial to their outstanding photocatalytic and photoelectrochemical activities.

Oxygen evolution reaction (OER) is a key process and the bottleneck in water splitting as the production of H_2 is severely constrained by the sluggish kinetics of OER.[1] Consequently, a substantial overpotential is required to drive the OER even with the benchmark precious catalysts such as IrO_2 and RuO_2.[2] However, these noble metals are costly, and are not suitable for large scale industrial applications. Therefore, tremendous efforts have been devoted to the development of efficient, abundant and inexpensive catalysts, such as oxides,[1c,2c,3] hydroxides,[1d,4,5] chalcogenides[6] and phosphides.[7]

As the benchmark materials for photocatalytic hydrogen production, cadmium chalcogenide based QR heterostructures, such as CdS-Pt,[8-12] CdS-PdX[9,13] and CdS-Au,[14,15] have been studied extensively over the years because they have appropriate band gap energies and efficient charge separation capabilities, which provide an adequate driving force for

hydrogen evolution. However, QR heterostructures containing both cadmium and noble metal suffer from a high toxicity and a high cost. For example, cadmium based QRs are highly toxic and their synthesis typically involves the use of toxic reagents such as phosphonic acid and phosphonic oxide.[16-19] The ideal alternatives to cadmium chalcogenides could be zinc chalcogenide QRs as they have an appropriate band gap energy and can be prepared by a phosphine-free protocol. Unfortunately, zinc precursors will form a lamellar structure in organic solution before they react with chalcogen anions, i.e. S^{2-}, Se^{2-} and Te^{2-}.[20] In such a case, the obtained zinc chalcogenide nanowires maintain their original lamellar structure, making them very hard to facilitate the anisotropic growth.[21-24] Although there are some reports presenting the synthesis of zinc chalcogenide QRs based on the epitaxial growth and thermodynamically driven material diffusion mechanisms,[21,25-29] it is still a challenge to prepare zinc chalcogenide QRs with good monodispersity.

Here, we report that nearly monodispere alloyed ZnS_xSe_{1-x} QRs can be facilely obtained from their polydisperse ZnSe nanowire counterparts in the presence of alkylthiol at elevated temperatures. This simple, but generic, approach produces nearly monodisperse heavy metal-free colloidal semiconductor QRs that could not be easily obtained by the conventional colloidal synthetic approaches. Without further calcination, the obtained QRs can be directly employed as photocatalysts for OER in water splitting. The alloyed ZnS_xSe_{1-x} QRs are noble- and heavy-metal-free, demonstrating both highly efficient catalytic activities of OER and enhanced photoelectrochemical performance.

To synthesize zinc chalcogenide QRs, we took the advantage of the ease with which zinc chalcogenide forms ultrathin nanowires while intentionally added alkylthiol as an external input during their growth at elevated temperatures. Our synthesis is based on a colloidal chemical synthetic route (see the scheme in **Figure 1**a). Figure 1b shows the schematic illustration of the formation of alloyed ZnS_xSe_{1-x} QRs: Starting with polydisperse ultrathin ZnSe nanowires, paired nanorods are formed in the presence of 1-dodecanethiol (DDT) via a

self-limited assembly mechanism;[29] then each two rod components of a paired rod form a single rod with a large diameter through intraparticle fusion, and finally the etching of DDT leads to the fromation of nearly monodisperse alloyed ZnS_xSe_{1-x} QRs. Transmission electron microscope (TEM) images (Figure 1c, Figure S1) and high angle annular dark field-scanning transmission electron microscopy (HAADF-STEM) (Figure 1d) image show the predominantly elongated features of the alloyed ZnS_xSe_{1-x} QRs with an aspect ratio of ~5. Statistics on the size of the alloyed QRs show the uniformity of both length (16.3±4.3nm) and diameter (3.6±0.7nm).

High-resolution TEM (HRTEM) characterization reveals high crystallinity with lattice fringes throughout the whole particles (Figure 1e). The lattice planes marked in Figure 1e are perpendicular to each other and the extracted lattice distances of 3.17Å and 3.35Å correspond to the (002) and (100) planes of the wurtzite structure. Fast Fourier transform (FFT) analysis of the selected area of a nanorod (red rectangle in Figure 1e and the inset) shows the crystallographic relations, corroborating the wurtzite structure. The derived lattice plane spacings of 3.17 Å (002) and 3.35Å (100) of QRs show a slight shrinkage with respect to the 3.25 Å (002) and 3.43 Å (100) planes of the standard wurtzite ZnSe (PDF#15-0105), suggesting that the obtained crystal lattices are constrained. We further conducted STEM-energy-dispersive X-ray spectroscopy (STEM-EDX) and X-ray diffraction (XRD) to elucidate the reason that is responsible for this shrinkage of the crystal lattices.

STEM-EDX element maps show that both Zn and Se are evenly distributed throughout the elongated QRs (Figure 1f). Since DDT has been intentionally added into the react system during the growth of the nanoparticles, we also acquired a STEM-EDX element map on S. The element map for sulfur clearly shows that a homogeneous distribution of S element throughout the nanoparticles is seen, indicating the formation of alloyed ZnS_xSe_{1-x} QRs. XRD analysis shows that the obtained QRs crystallize into wurtzite structure (Figure 1g) and the

sharp peak of the (002) plane confirms the long axis direction. All diffraction peaks shift to large angles, indicating the obtained QRs have smaller crystal lattices in regard to the standard wurtzite ZnSe. The results on XRD measurement are consistent with our crystallographic interpretations based on the HRTEM characterization, in which smaller lattice plane spacings are derived, corroborating the formation of alloyed ZnS_xSe_{1-x} QRs.

In the next step, we combine TEM characterization with optical absorption spectroscopy (**Figure 2**) to reveal the growth mechanism of alloyed ZnS_xSe_{1-x} QRs, as schematically shown in Figure 1b. Polydisperse ZnSe nanowires (length 80±37nm, width 2.4±0.6nm, Figure 2a) have been synthesized using a literature method (see Supporting Information for details).[21] The obtained ZnSe nanowires were separated from the crude solution by dissolving into chloroform and precipitating by methanol with the aid of centrifugation. Subsequently they were re-dissolved into oleylamine solution, in which zinc precursor stock solution was added to prevent the ripening of the ZnSe nanowires at elevated temperatures. DDT was swiftly injected into the react mixture when the temperature of the system reached 260 ^{o}C. Within 30 minutes at 260-280 ^{o}C, TEM measurements on aliquots show the initial pairing of nanowires leads to paired rod (Figure 2b), which subsequently undergo intraparticle fusion to form thick QRs (Figure 2c), and finally polydisperse QRs break down, producing nearly monodisperse alloyed ZnS_xSe_{1-x} QRs due to DDT etching (Figure 2d).

Starting with long ZnSe nanowires (length 80±37nm, width 2.4±0.6 nm, Figure 2a), the length of the nanoparticles slightly shrunk to 69±32nm while the width increased to 6.3±0.8 nm as the reaction evolved for 30 seconds at 260 ^{o}C (Figure 2b) in the presence of DDT. The large increase of the width of the nanoparticles from 2.4±0.6 nm to 6.3±0.8 nm is associated with the pairing of the proceeding ZnSe nanowires (Figure 2b). The diffraction peaks of the sample in Figure 2b show a small shift of 0.17 degrees to large angles with respect to the standard XRD pattern of wurtzite ZnSe (Figure S2, Suppporting Information). After the reaction was evolved for 30 seconds at 260 ^{o}C, it was heated to 280 ^{o}C within four minutes.

As the reaction evolved for 5 minutes at 280 °C, the gap between two rod components of each paired rod vanishes, and therefore two rod components form a thick QR by intraparticle fusion (Figure 2c). Accordingly, the length of the obtained QRs becomes 54±27nm and their width is 3.9±0.9nm, being much smaller compared with the width of the proceeding paired rods, which is 6.3±0.8 nm. Further reaction at this temperature for 30 minutes produced nearly monodisperse QRs (length 20±6 nm, width 3.9±0.4 nm) (Figure 2d). The absorption onset was red-shifted from 345 nm to 398 nm, 401 and then to 403 nm after 30 seconds at 260 °C, 5 minutes and 30 minutes at 280 °C, respectively (Figure 2e), being consistent with the increase in the width of the produced nanoparticles. The shift of diffraction peaks of the obtained products showed a shift from 0.23 and 0.60 degrees as the reaction evolved for 5 min and 30 min at 280 °C, respectively (Figure S2, Suppporting Information). This continuous shift corresponds to the shrinking of the lattice spacings (Table S1). EDX measurement on these aliquots reveals a decreasing trend of the chemical compostion of Se while that of S is gradually increasing as the reaction proceeds (Figure 2f), reaching a ratio of ~2:1 for S:Se for the final products of alloyed ZnS_xSe_{1-x} QRs. This clearly shows that some of the Se^{2-} anions in ZnSe is gradually substituted by S^{2-} as the reaction proceeds in the presence of DDT at elevated temperatures, leading to the spontaneous formation of nearly monodisperse alloyed ZnS_xSe_{1-x} QRs.

Except for the original ZnSe nanowires, all the aliquots and final products show detectable photoluminescence with a trap state broad emission band at longer wavelengths due to the imperfect passivation of the obtained nanoparticles (Figure 2e). Our previous studies on the synthesis of ZnSe nanoparticles demonstrate that ZnSe nanowires retain their original morphology at elevated temperatures when zinc precursor is added into the reaction mixture.[21] Herein, to synthesize nearly monodisperse QRs from polydisperse nanowires, we took the advantage of this fact while conducted the experiments under identical synthetic conditions except that DDT was intentionally added into the reacting solution at elevated

temperatures, i.e. 260-280 °C. ZnSe nanowires retain their original morphology because the particle ripening is significantly hindered in the presence of zinc precursor (Figure S3b, Supporting Information).[21] However, they converted into long and thick ZnSe QRs through Ostwarld ripening in the absence of both zinc precursor and DDT (Figure S3d, Supporting Information),[21] as further confirmed by absorption spectra (Figure S3e, Suppporting Information) and XRD (Figure S3f, Suppporting Information) measurements. The significant difference between the products obtained in the absence of (Figure S3d, Supporting Information) and in the presence of DDT (Figure S3c, Suppporting Information) unambiguously corroborates the essential role of DDT that leads to the initial pairing of nanowires at the early stage and the formation of short alloyed QRs at the later stage of the reaction due to the alkylthiol etching.

We further conducted three groups of parallel syntheses in order to elucidate how the reaction temperature (Figure S4a-c, Suppporting Information), amount (Figure S4d-f, Suppporting Information) and type of sulfur sources (Figure S4g-i, Suppporting Information) will affect the formation of alloyed QRs and how to gain better control on their size distribution. We conducted three parallel syntheses at or slightly below the temperature of the boiling point of DDT, which is 280 °C.[30] As soon as DDT was injected into the react solution, oleylamine ligand binding on the surface of nanoparticles is likely replaced by DDT because DDT is a stronger binding ligand than oleylamine. The reaction at 250 °C for 30 minutes in the presence of DDT (Figure S4a, Supporting Information) leads to slightly thick nanowires only (length 90±24nm, width 3.9±0.7 nm, Figure S5a, 5b, Supporting Information), indicating this reaction temperature is too low to ensure the high capability of etching of DDT. Another experiment conducted at 260 °C (Figure S4b, Suppporting Information) prouded a mixture consisting of short QRs and long nanowires with a large size distribution (length 21±13nm, width 4.0±0.7 nm, Figure S5c, 5d, Supporting Information). The third experiment conducted at 280 °C (Figure S4c, Supporting Information) produces nearly monodisperse QRs (length

17±4nm, width 4.4±0.8 nm, Figure S5e, 5f, Supporting Information). These results clearly demonstrate that nearly monodisperse QRs were obtained from polydisperse nanowires by alkylthiol etching. Moreover, DDT shows a high etching capability only when the temperature of the reaction system is close to its boiling point. This is easy to understand since, at such an elevated temperature, the surface binding ligand of DDT becomes more liable and is easy to be liberated from the surface of the nanoparticles, which in turn, makes the nanoparticles less stable and break down, therefore producing nearly monodisperse short QRs.

To gain better control on the size distribution of the QRs, we conducted a second group of three parallel syntheses in the presence of different amounts of DDT. In such syntheses, different amounts of DDT (0.3 mL, 0.5 mL and 1 mL, Figure S4d-f, Supporting Information) were swiftly injected into the solution at 260 °C and then the mixture was increased to 280 °C in four minutes. Final products were obtianed as the reaction proceeded for 30 minutes at 280 °C. All of the above syntheses produced nearly monodisperse QRs with different size (See sizing historgrams in Figure S6, Supporting Information). These results demonstrate that size control of ZnSe QRs can be achieved through the optimization of the amount of DDT.

We further use other sulfur sources, including 1-hexadecanethiol (HDT), 1-octadecanethiol (ODT), and bis(trimethylsilyl) sulfide ($(TMS)_2S$) (Figure S4g-i, Supporting Infomration), to conduct the syntheses while keeping all of the other synthetic conditions the same. All syntheses produces nearly monodisperse QRs, demonstrating the essential role of akylthiol in the formation of monodisperse alloyed QRs from monodisperse nanowires.

To demonstrate the generality of this synthetic approach, it was further expended to synthesize QRs of other zinc chalcogenides, including ZnS, from polydisperse ZnS nanowires. ZnS nanowires with a diameter of ~2 nm (Figure S7a, Supporting Information) were synthesized using a literature method[21] and the absorption spectrum shows the first exciton absorption peak at 288 nm (Figure S7c, Supporting Information). After the reaction evolved

for 30 minutes at 280 °C, ZnS QRs with a diameter of 3.5 nm were produced (Figure S7b, Supporting Information). The red shift of the absorption onset from 288 nm to 304 nm is consistent with the increase of diameter of ZnS QRs (Figure S7c, Supporting Information). XRD patterns of the obtained ZnS QRs match wurtzite structure and the sharp peak of the (002) plane confirmed the preferential elongation of the QRs (Figure S7d, Supporting Information).

The obtained alloyed $ZnS_{2/3}Se_{1/3}$ QRs were used as the catalysts to test their photocatalytic and PEC performances. Notably, alloyed $ZnS_{2/3}Se_{1/3}$ QRs can be directly adopted as photocatalysts for water splitting without further calcination. The photocatalytic water oxidation of the as-prepared samples was conducted under ultraviolet light irradiations using persulfate ($S_2O_8^{2-}$) as a sacrifice oxidant for the reduction reaction, whereas tris(2,2′-bipyridine) ruthenium(II) (Ru-$(bpy)_3^{2+}$) was used as the one-electron oxidant photosensitizer to promote multiple-electron water oxidation kinetics and avoid excessive driving potentials (See Supporting Informaiton for details). To elucidate the water oxidation mechanism shown schematically in **Figure 3**a, experiments without one of above three components, i.e. photosensitizer, catalysts and sacrificial agents, were performed, and all experiments show almost no activity (Figure 3b). This suggests that the presence of all three components, $ZnS_{2/3}Se_{1/3}$, $[Ru(bpy)_3]^{2+}$ and $Na_2S_2O_8$, are indispensable for the whole oxygen evolution reaction. As shown in the scheme of water oxidizaiton (Figure 3a), two out of four $[Ru(bpy)_3]^{2+}$ are converted into their excited state, $2[Ru(bpy)_3]^{2+*}$ by illumination through the metal-to-ligand charge transfer (MLCT). Photoinduced electron transfer from $2[Ru(bpy)_3]^{2+*}$ to $2S_2O_8^{2-}$ produces $2Ru(bpy)_3^{3+}$, SO_4^{2-}, and $SO_4^{•-}$.[31] The produced $SO_4^{•-}$ can oxidize $[Ru(bpy)_3]^{2+}$ to produce two equiv of $2Ru(bpy)_3^{3+}$.[32] In the meanwhile, electrons and holes are generated and separated by the catalysts of alloyed $ZnS_{2/3}Se_{1/3}$ QRs with illumination, and then the photogenerated electrons are transferred to $[Ru(bpy)_3]^{3+}$ that regenerates $[Ru(bpy)_3]^{2+}$ while water is oxidized, leading to O_2 evolution.

A control experiment utilizing ZnS, ZnSe and alloyed $ZnS_{2/3}Se_{1/3}$ QRs as the photocatalysts show that the alloyed QRs demonstrate increased OER activity (Figure 3b). Figure 3c presents the time dependent oxygen concentration using the synthesized catalysts under three cycles running. The catalyst displays an efficient OER yield of 3000 µmol g^{-1} h^{-1} during the first 30 min irradiation and reached the flat at about 1 hour. The apparent quantum efficiency (AQE) under irradiation for $ZnS_{2/3}Se_{1/3}$ photocatlysts was measured to be approximately 13.3% ($\lambda = 380$ nm) and 0.33% ($\lambda = 420$ nm) (See Supporting Information for details). It is also observed that the reaction rate showed an inevitable slowdown trend at the second running test and stabilized at the third cycle test, which will be further discussed in the following sections.

QRs-sensitized TiO_2 substrates were prepared and acted as the photoanodes for PEC measurement. Figure 3d and Figure S8 compare the current–voltage curves of the composites under illumination and dark condition, respectively. The suitable band gap alignments between alloyed QRs and TiO_2 ensure the efficient electron hole transport (Figure S9, Supporting Information). As a result, all the sensitized photoanodes present significantly enhanced anodic photocurrent densities with the order $ZnS_{2/3}Se_{1/3}/TiO_2$ > $ZnSe/TiO_2$ > ZnS/TiO_2 > TiO_2 upon illumination. Furthermore, all the sensitized photoanodes show the cathodal shift onset potentials and the alloyed $ZnS_{2/3}Se_{1/3}$ QRs sensitized photoanode displays the largest shift, demonstrating the highest potential for water oxidation among all QRs-sensitized TiO_2 photoanodes. The detailed oxidation kinetics of these QRs will be further discussed in the DFT section below. As shown in Figure 3e, the transient photo response of the photoanodes were assessed by measuring i-t curves at an open circuit potential. Prompt and steady photocurrent responses can be captured on the photoanodes during on and off cycles of illumination. Consistantly, $ZnS_{2/3}Se_{1/3}$ QRs sensitized photoanode presents the most obvious enhancement of the photocurrent densities, which is 4.5 times higher than that of pristine TiO_2 anode (Figure 3e). The enhancement of the photocurrent densities for ZnSe QRs

sensitized photoanode is 2.8 times higher than that of pristine TiO_2 anode whereas those for

ZnS QDs sensitized photoanode does not show evicently enhanced photocurrent densities

(Figure 3e). The amount of O_2 oxidized by $ZnS_{2/3}Se_{1/3}/TiO_2$ and TiO_2 photoanodes under the

irradiation were in-situ probed through the potentiostatic method. As shown in Figure 3f, the

amount of experimentally quantified O_2 of $ZnS_{2/3}Se_{1/3}/TiO_2$ was nearly 90% Faradic

efficiency (FE) of theoretically calculated value. The photocurrent density changes during the

FE test were also obtained as a function of illumination time (Figure S10).

We further conducted the electrochemical active surface area (EASA) test to probe the

difference of the surface active sites of ZnS, ZnSe and alloyed $ZnS_{2/3}Se_{1/3}$ QRs, wherein

double-layer capacitance (Cdl) of the samples were tested from 0.705 to 0.855 V at scan rates

of 10, 20, 30, 40, and 60 mV s^{-1} (Figure S11, Supporting Information). The corresponding

capacitive current densities at 0.75 V were plotted as a function of scan rate (Figure S10d,

Supporting Information). The slope of the fitted line equals twice the value of Cdl and

represents EASA. The alloyed $ZnS_{2/3}Se_{1/3}$ QRs show a higher electrochemically EASA, i.e.

0.288 mF cm^{-2}, which is about two times higher than that of ZnSe (0.139 mF cm^{-2}) and thirty-

two times higher than that of ZnS (0.009 mF cm^{-2}) QRs. This result clearly shows that

abundant surface active sites were introduced to the alloyed $ZnS_{2/3}Se_{1/3}$ QRs by etching of

DDT during the formation of alloyed QRs.

A variety of characterizations on the alloyed $ZnS_{2/3}Se_{1/3}$ QRs after photocatalytic and

PEC tests were conducted to gain insights on the deceased photocatalytic activity after two

times of running as well as to eleucidate their stability. **Figure 4**a-c and 4d-f compared the

electron miscroscopy images of alloyed $ZnS_{2/3}Se_{1/3}$ QRs after photocatalytic and

photoelectrochemical tests, respectively. The HAADF-STEM (Figure 4a, 4d), TEM (Figure

4b, 4e), HRTEM and associated FFT analysis of the selected area (Figure 4c, 4f, Figure S12,

Supporting Information), and XRD (Figure S13, Supporting Information) measurements show

that the $ZnS_{2/3}Se_{1/3}$ QRs after the OER and PEC tests retain their original morphology and

show good crystallinity, with evident lattice fridges indexed into wurtzite structure (Figure 4c, 4f, Figure S12, Supporting Information). STEM-EDX analysis show that all elements including zinc, selenium and sulfur in the $ZnS_{2/3}Se_{1/3}$ QRs after OER and PEC tests are distributed evenly throughout the whole nanoparticles (Figures S14, S15, Supporting Information), further confirming the confirm their good stability.

High-resolution X-ray photoelectron spectroscopy (XPS) was used to examine the binding environment in QRs. Notably, the survey spectra of the samples after OER and PEC tests reveal that the binding energies for Zn 2p (Figure 4g), Se 3d (Figure 4h), Se 3p and S2p (Figure 4i) show a slight shift to the higher energy in comparison with those of the original QRs. This tiny shift of the binding energies is likely attributed to the interaction between Se (Zn, S) and other atoms, as previously observed in Au/ZnSe.[33] Except for Se, all elements are present solely as Zn(+2) and S(-2), since no satellites of these elements with other oxidation states were observed.[34,35] However, a close inspection on the 3d region of Se of the QRs after OER and PEC tests shows that the spectra in this region can be well-fitted by two doublets of selenium species (Figure 4h) with an integrated intensity ratio and energy difference for Se $3d_{5/2}$ and Se $3d_{3/2}$ being 3:2 and 0.83 eV, respectively, which are in good agreement with the literature values.[36] The Se $3d_{5/2}$ binding energy at 56.9 eV (blue fitted curves in Figure 4h) for the new selenium species matches well with that of $Na_2Se(S_2O_3)_2$,[37] which may form on the surface of $ZnS_{2/3}Se_{1/3}$ QRs during the OER and PEC tests. The determination of XPS spectra of selenium in the 3p region is complicated due to the overlap with S peaks in 2p region (Figure 4i). However, the positions of the main components of S $2p_{3/2}$ (162.03 eV) and S $2p_{1/2}$ (163.15 eV) confirm the presence of sulfides S^{2-}.[38] The interpretation of the XPS spectra is consistent with our observation on the decreased activity of the catalysts after two circles running. This is because that the surface active sites of alloyed $ZnS_{2/3}Se_{1/3}$ QRs has been stabilized after the first run, during which $Na_2Se(S_2O_3)_2$ may form on the surface of $ZnS_{2/3}Se_{1/3}$ QRs and thus partially blocks the surface active sites.

To gain further insights on the photocatalytic and PEC activities of alloyed ZnS_xSe_{1-x} QRs, in particular to elucidate the reason why alloyed QRs process increased catalytic activity over their counterparts such as both pure ZnS and ZnSe QRs, we employed the first-principles method based on density functional theory to evaluate the catalytic activity of alloyed ZnS_xSe_{1-x} QRs (see Supporting Information for details).[39-42] We used two different stoichiometric ratios of the alloyed QRs, i.e. $ZnS_{0.5}Se_{0.5}$ as the intermediate, and $ZnS_{2/3}Se_{1/3}$ as the final product, to perform the simulations. Results shows that this ratio only change the amount of the surface active sites alloyed QRs but does not alter their intrinsic properties for catalysis. As compared in **Figure 5**a, Figures S16, S17 and Table S2 in Supporting Information, the band gap of QRs is gradually shifting to a higher energy as the composition of sulfur increases, but clearly their valance band edges are lower than the H_2O/O_2 level and their conduction band edges are higher than the H_2/H_2O level, suggesting their potential capability for OER. The (100) and (110) surfaces are calculated to be the most stable surfaces with a similar surface energy. This is consistent with the experimental structural characterization, in which (100) surface is the dominant surface for the wurtzite QRs, and therefore the OER Gibbs free energy calculations were based on this surface.

OER involving four electron transfers can be treated by four elementary steps, during which intermediates of *OH, *O and *OOH are generated (Figure 5b, 5c). The configurations of adsorbed redox species on $ZnS_{0.5}Se_{0.5}$ (100) surface were depicted in Figure 5c. The OER energy barriers for generation of *OH, *O and *OOH species on active Zn sites of (100) surface, as schematically illustrated in Figure 5b, were calculated and shown in Table S3, Supporting Information. The energy barriers are associated with Gibbs free energy changes during the four steps (ΔG_1-ΔG_4), based on which the energy diagrams are obtained. The high uphill/endothermic energy profiles for the deprotonation of H_2O (*+$H_2O\rightarrow$ *OH+H^++e^-, step 1) and *OH (HO*$\rightarrow$O*+H^++e^-, step 2) on ZnS (100) indicate a high overpotential and the low activity of ZnS. ΔG_1 of ZnSe is much lower than ZnS, suggesting a higher activity of

ZnSe. However, ΔG_2 of ZnSe is still large. ΔG_1, ΔG_2 and ΔG_3 of the alloys are much lower than those of ZnS and ZnSe, which leads to a very low overpotential. Step 4 (*OOH $\rightarrow$ O_2+H^++e^-) are downhill/exothermic for all materials, suggesting that it is effortless to proceed and *OOH will convert to O_2 automatically.

As regard to OER activity, it is straightforward to predict a higher activity of ZnSe compared to ZnS based on the analysis above, and we should expect an intermediate OER activity for the alloyed ZnS_xSe_{1-x} QRs. However, very high active Zn sites were found on $ZnS_{0.5}Se_{0.5}$ (100) and $ZnS_{2/3}Se_{1/3}$ (100) surface. Figure 5d and 5e shows the differential charge density at an isosurface value of 0.004 e/$Å^3$ for *O species absorbed on $ZnS_{0.5}Se_{0.5}$ (100) surface. *O gains additional charge by forming a chemical bond with the neighbouring Se, which stabilizes *O on the surface and reduced the energy barrier ΔG_2 (HO*$\rightarrow$O*+H^++e^-). A close inspection reveals the key role of Se ions in promoting the OER activity of Zn surface site that is coordinated by two Se ions and one S ion. The Se at the second nearest neighbour distance to Zn can form Se-O bonding with the adsorbed O on Zn (and there is no barrier as can be seen from nudged elastic band calculations in Movie S1), which greatly reduces the reaction free energy of step 3 of OER. In such as a case, once *OH is deprotonated, the *O species tend to relax itself by forming an additional bond with the neighbouring Se anion, which comes at no energy barrier (Movie S1). This can be understood since Se-p electrons that dominate the occupied states close to Fermi level is chemically active. While, this cannot occur for surface Zn site coordinated completely with three Se ions, for which the Zn ion forms a strong Zn-O bonding. Therefore, the alloyed ZnS_xSe_{1-x} QRs with more active Zn site show a higher OER activity than pure ZnS and ZnSe.

In conclusion, we have developed an wet-checmial approach that leads to spontaneous formation of nearly monodisperse alloyed ZnS_xSe_{1-x} QRs from polydisperse ZnSe nanowires by the etching of alkylthiol. The obtained alloyed QRs can be directly used for OER and PEC

14

tests without calcination. Compared with pure ZnS and ZnSe, alloyed ZnS_xSe_{1-x} QRs show enhanced OER acitivity in water splitting and PEC activities because of the highly active Zn sites on the (100) surface and reduced water oxidation energy barrier, as revealed by DFT simulations. This work not only sheds light on the construction of one-dimensional nanostructures but also provides a basis for earth abunant and environmental friendly photocatalysts.

Experimental Section

The experimental details on the preparation of zinc stock solution, alloyed ZnS_xSe_{1-x} QRs, their morphology and structural characterizations, optical spectroscopy, XRD, photocatalytic and photoelectrochemical tests, ESAS test, DFT simulations are provided in the Supporting Information.

Supporting Information

Supporting Information is available from the Wiley Online Library or from the author.

Acknowledgement

References

[1]   a) R. D. L. Smith, M. S. Prévot, R. D. Fagan, Z.P. Zhang, P. A. Sedach, M. K. J. Siu,

        M. Kit, J. Siu, S. Trudel, C. P. Berlinguette, *Science* **2013**, *340*, 60; b) J. Wang, F. Xu,

        H. Y. Jin, Y. Q. Chen, Y. Wang, *Adv. Mater.* **2017**, *29*, 1605838; c) X. F. Lu, L. F. Gu,

        J. W. Wang, J. X. Wu, P. Q. Liao, G. R. Li, *Adv. Mater.* **2017**, *29*, 1604437; d) R. Liu,

        Y. Wang, D. Liu, Y. Zou, S. Wang, *Adv. Mater.* **2017**, *29*, 1701546.

[2]   a) T. R. Cook, D. K. Dogutan, S. Y. Reece, Y. Surendranath, T. S. Teets, D. G. Nocera,

        Chem. Rev. **2010**, *110,* 6474; b) Y. P. Liu, Q. J. Li, R. Si, G. D. Li, W. Li, D. P. Liu, D.

        J. Wang, L. Sun, Y. Zhang, X. X. Zou, *Adv. Mater.* **2017**, *29*, 1606200; c) L. H.

        Zhuang, L. Ge, Y. S. Yang, M. R. Li, Y. Jia, X. D. Yao, Z. H. Zhu, *Adv. Mater.* **2017**,

        29, 1606793.

[3]   Y. Zheng, Y. Jiao, Y. Zhu, Q. Cai, L. H. Li, Y. Han, Y. Chen, S. Qiao, *J. Am. Chem.*

        Soc. **2017**, *139,* 3336.

[4]   F. Song, X. Hu, *Nat. Commun.* **2014**, *5,* 4477.

[5]   a) X. Lu, C. Zhao, *Nat. Commun.* **2015**, *6,* 6616; b) J. Wang, W. Cui, Q. Liu, Z. Xing,

        A. Asiri, X. Sun, *Adv. Mater.* **2016**, *28*, 215.

[6]   a) C. Tang, N. Cheng, Z. Pu, W. Xing, X. Sun, *Angew. Chem., Int. Ed.* **2015**, *127,*

        9483; b) H. Zhu, J. Zhang, R. Yanzhang, M. Du, Q. Wang, G. Gao, J. Wu, G. Wu, M.

        Zhang, B. Liu, *Adv. Mater.* **2015**, *27*, 4752.

[7]   a) N. Jiang, B. You, M. Sheng, Y. Sun, *Angew. Chem., Int. Ed.* **2015**, *127,* 6349; b) R.

        Wang, X. Y. Dong, J. Du, J. Y. Zhao, S. Q. Zang, *Adv. Mater.* **2018**, *30*, 1703711.

[8]   a) L. Amirav, A. P. Alivisatos, *J. Phys. Chem. Lett.* **2010**, *1,* 1051; b) G. Dukovic, M.

16

G. Merkle, J. H. Nelson, S. M. Hughes, A. P. Alivisatos, *Adv. Mater.* **2008**, *20*, 4311.

[9]   a) S. E. Habas, P. Yang, T. Mokari, *J. Am. Chem. Soc.* **2008**, *130,* 3294; b) E. Elmalem, A. E. Suanders, R. Costic, A. Salant, U. Banin, *Adv. Mater.* **2008**, *20*, 4312.

[10]   H. Schlicke, D. Ghosh, L. Fong, H. L. Xin, H. Zheng, A. P. Alivisatos, *Angew. Chem., Int. Ed.* **2013**, *52,* 980.

[11]   L. J. Hill, M. M. Bull, Y. Sung, A. G. Simmonds, P. T. Dirlam, N. E. Richey, S. E. DeRosa, I.-B. Shim, D. Guin, P. J. Costanzo, N. Pinna, M.-G. Willinger, W. Vogel, K. Char, J. Pyun, *ACS Nano* **2012**, *6,* 8632.

[12]   M. Berr, A. Vaneski, A. S. Susha, J. Rodríguez-fernández, M. Döblinger, F. Jäckel, A. L. Rogach, J. Feldmann, *Appl. Phys. Lett.* **2010**, *97,* 093108.

[13]   Y. Shemesh, J. E. Macdonald, G. Menagen, U. Banin, *Angew. Chem., Int. Ed.* **2011**, *123,* 1217.

[14]   Y. Ben-shahar, F. Scotognella, I. Kriegel, L. Moretti, G. Cerullo, E. Rabani, U. Banin, *Nat. Commun.* **2016,** *7,* 10413.

[15]   Y. Ben-shahar, F. Scotognella, N. Waiskopf, I. Kriegel, S. D. Conte, G. Cerullo, U. Banin, *Small* **2015**, *11,* 462.

[16]   X. Peng, L. Manna, W. Yang, J. Wickham, E. Scher, A. Kadavanich, A. P. Alivisatos, *Nature* **2000**, *404*, 59.

[17]   D. J. Milliron, S. M. Hughes, Y. Cui, L. Manna, J. Li, L.-W. Wang, A. P. Alivisatos, *Nature* **2004**, *430*, 190.

[18]   L. Carbone, C. Nobile, M. De. Giorgi, F. D. Sala, G. Morello, P. Pompa, M. Hytch, E. Snoeck, A. Fiore, I. R. Franchini, M. Nadasan, A. F. Silvestre, L. Chiodo, S. Kudera, R. Cingolani, R. Krahne, L. Manna, *Nano Lett.* **2007,** *7,* 2942.

[19]   D. V. Talapin, J. H. Nelson, E. V. Shevchenko, S. Aloni, B. Sadtler, A. P. Alivisatos, *Nano Lett.* **2007**, *7,* 2951.

[20]   J. Zhang, C. Rowland, Y. Liu, H. Xiong, S. Kwon, E. Shevchenko, R. D. Schaller, V. B.

Prakapenka, S. Tkachev, T. Rajh, *J. Am. Chem. Soc.* **2015**, *137, 742.*

[21] G. Jia, U. Banin, *J. Am. Chem. Soc.* **2014**, *136,* 11121.

[22] S. Acharya, S. Efrima, *J. Am. Chem. Soc.* **2005**, *127,* 3486.

[23] A. B. Panda, S. Acharya, S. Efrima, *Adv. Mater.* **2005**, *17*, 2471.

[24] Y. Wang, Y. Zhou, Y. Zhang, W. E. Buhro, *Inorg. Chem.* **2015**, *54,* 1165.

[25] J. Zhang, S. Jin, H. C. Fry, S. Peng, E. Shevchenko, G. P. Wiederrecht, T. Rajh, *J. Am. Chem. Soc.* **2011,** *133,* 15324.

[26] S. Acharya, S. Sarkar, N. Pradhan, *J. Phys. Chem. C* **2013**, *117,* 6006.

[27] T. Yao, Q. Zhao, Z. Qiao, F. Peng, H. Wang, H. Yu, C. Chi, J. Yang, *Chem. Eur. J.* **2011**, *17*, 8663.

[28] B. Ji, Y. E. Pan, U. Banin, *ACS Nano* **2017,** *11,* 7312.

[29] G. Jia, A. Sitt, G. B. Hitin, I. Hadar, Y. Bekenstein, Y. Amit, I. Popov, U. Banin, *Nat. Mater.* **2014**, *13*, 301.

[30] B. A. Korgel, N. Zaccheroni, D. Fitzmaurice, *J. Am. Chem. Soc.* **1999**, *121*, 3533.

[31] D. Hong, Y. Yamada, T. Nagatomi, Y. Takai, S. Fukuzumi, *J. Am. Chem. Soc.* **2012**, *134*, 19572.

[32] A. L. Kaledin, Z. Huang, Y. V. Geletii, T. Lian, C. L. Hill, D. G. Musaev, *J. Phys. Chem. A* **2010**, *114*, 73.

[33] W.-J. Bao, J. Li, J. Li, Q.-W. Zhang, Y. Liu, C.-F. Shi, X.-H. Xia, *Anal. Chem.* **2018**, *90*, 3842.

[34] J. E. B. Katari, V. L. Colvin, A. P. Alivisatos, *J. Phys. Chem.* **1994**, *98*, 4109-4117.

[35] V. Lesnyak, C. George, A. Genovese, M. Prato, A. Casu, S. Ayyappan, A. Scarpellini, L. Manna, *ACS Nano* **2014**, *8*, 8407-8418.

[36] W. Chen, A. Kahn, P. Soukiassian, P. S. Mangat, J. Gaines, C. Ponzoni, D. Olego, *Phys. Rev. B* **1994**, *49*, 10790.

[37] U. Weser, G. Sokolowski, W. Pilz, *J. Electron Spectrosc. Relat. Phenom.* **1977**, *10*, 429.

[38]   C. J. Vesely, D. W. Langer, *Phys. Rev. B* **1971**, *4*, 451.

[39]   G. Kresse, D. Joubert, *Phys. Rev. B* **1999**, *59*, 1758.

[40]   P. E. Blöchl, *Phys. Rev. B* **1994**, *50*, 17953.

[42]   G. Kresse, J. Furthmüller, *Phys. Rev. B* **1996**, *54*, 11169.

[43]   G. Kresse, J. Hafner, *Phys. Rev. B* **1993**, *48*, 13115.
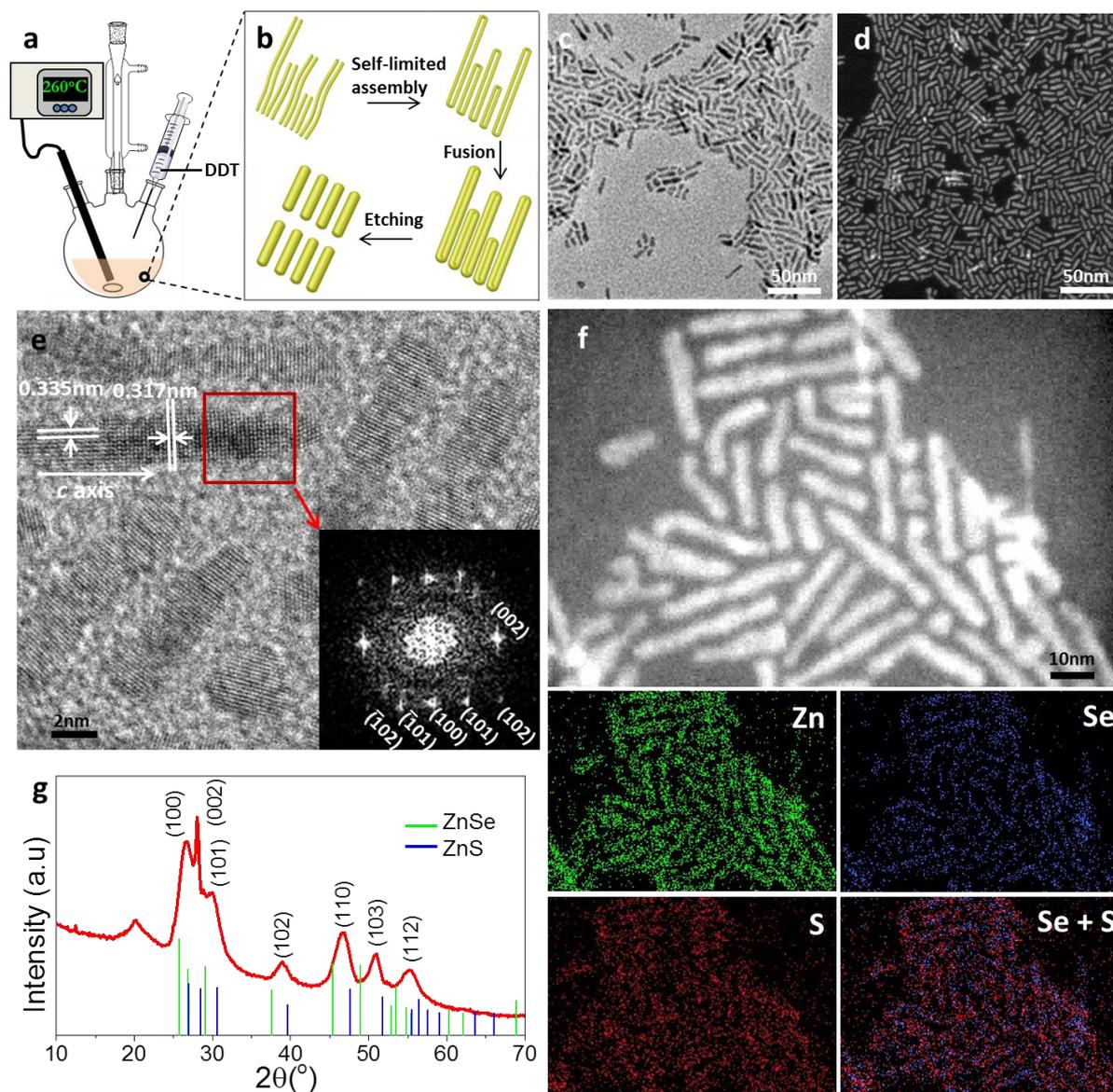
Figure 1. a) Scheme of the experimental setup. b) Schematic illustration of the formation of QRs. c) TEM image. d) STEM image. e) HRTEM image of QRs. Inset is FFT of selected areas of alloyed ZnS_xSe_{1-x} QRs, revealing the crystallographic relations. White lines indicate the orientation of selected crystal planes and arrow shows the orientation of long axis of QRs. f) HAADF-STEM image and STEM-EDX element maps. g) XRD pattern of QRs. Standard XRD patterns for both wurtzite ZnSe (PDF#15-0105) and ZnS (PDF#36-1450) were given for reference.
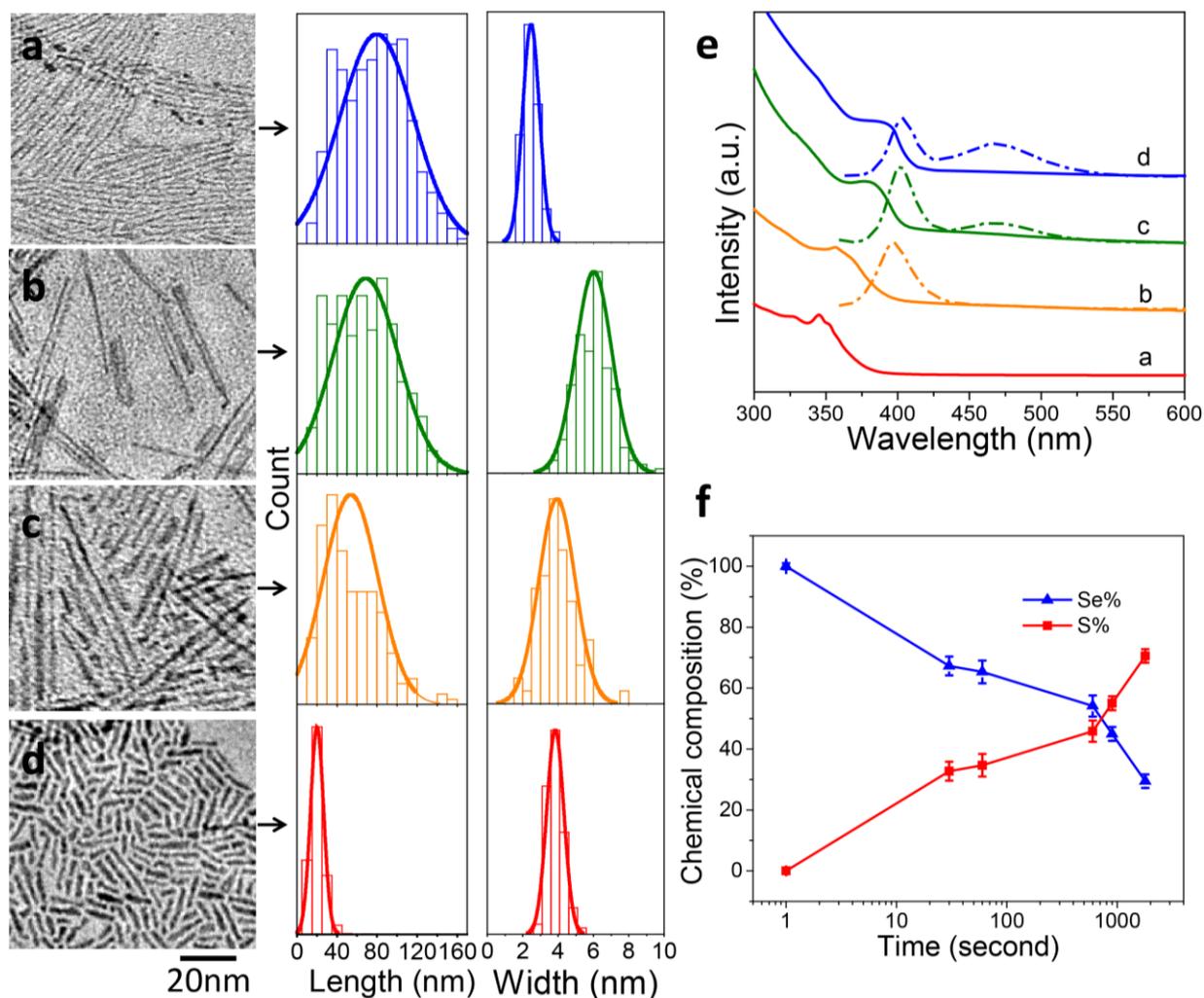
Figure 2. TEM images, size histograms, absorption and luminescence spectra of the aliquots and final products. a) original ZnSe nanowires, b-d) ZnSe QRs evolved from ZnSe nanowires after b) 30 seconds at 260 ºC, c) 5 minutes at 280 ºC, and d) 30 minutes at 280 ºC. The sizing histograms on length and width were shown on the righ-hand side of each TEM image. e) Absorption (solid line) and photolumiescence spectra (dash dotted line) of the nanoparticles. The original ZnSe nanowires do not show any detectable luminescence so the luminescence spectrum is not included in e). f) Chemical composition of Se (%) and S (%) of alloyed ZnS_xSe_{1-x} nanoparticles as a function of reaction time. Points in f) correspond to the original ZnSe nanowires, five aliquots, which were taken after the reaction evolved for 30 seconds at 260 ºC, 1 minutes at 280 ºC, 10 minutes at 280 ºC, 15 minutes at 280 ºC, and 30 minutes at 280 ºC.
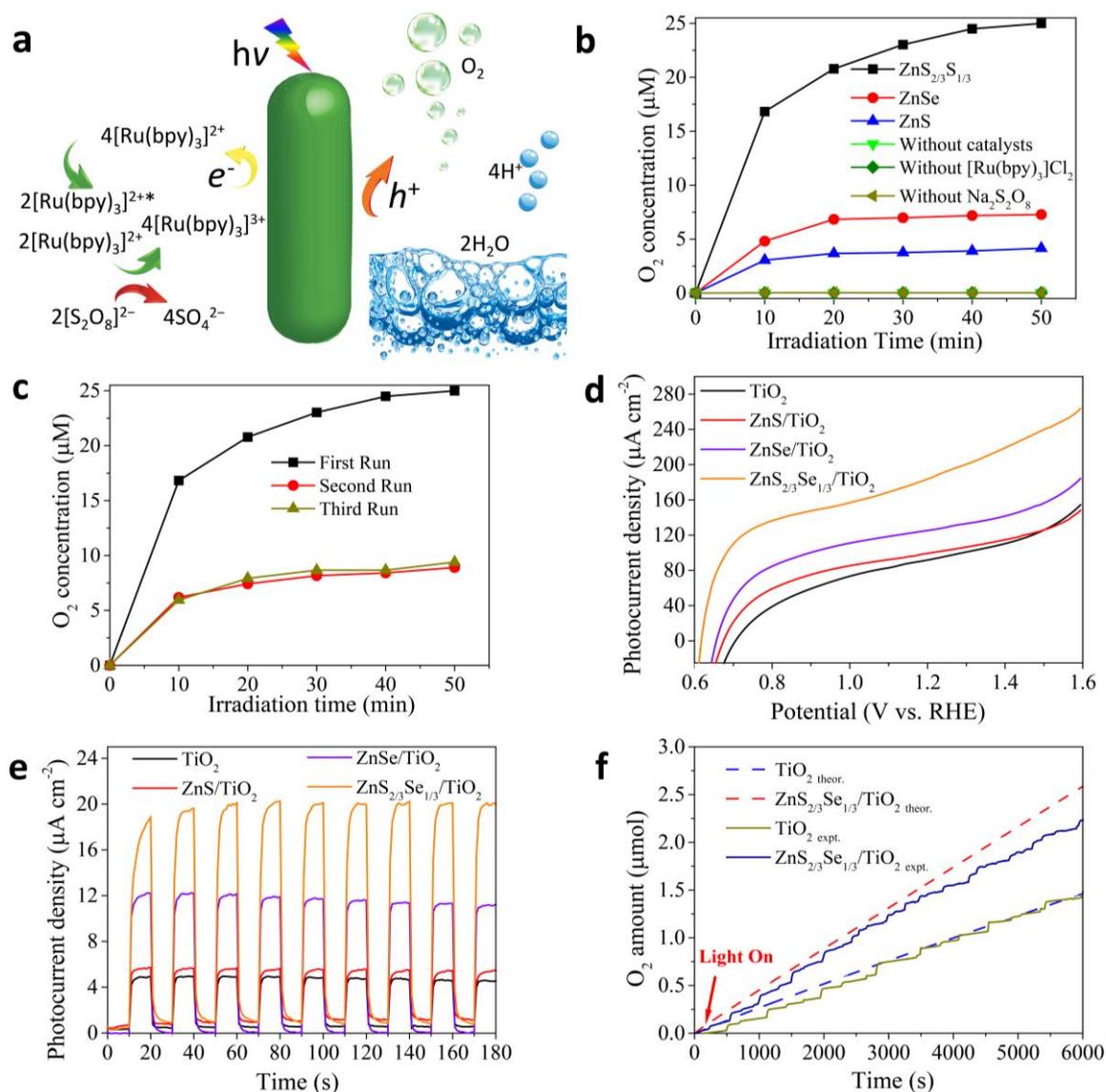
Figure 3. a) Schematic illustration of the water oxidation catalyzed by alloyed $ZnS_{2/3}Se_{1/3}$ QRs in the presence of $[Ru(bpy)_3]^{2+}$ and $Na_2S_2O_8$. b) Comparison of water oxidation using ZnS, ZnSe and alloyed $ZnS_{2/3}Se_{1/3}$ QRs as the catalysts. It also shows the control experiment conducted without one the three components, i.e. $ZnS_{2/3}Se_{1/3}$, $[Ru(bpy)_3]^{2+}$, and $Na_2S_2O_8$. c) Time dependent oxygen concentration using the synthesized catalysts under three cycles running. d) Current-voltage curves of the composites under illumination. e) i-t curves at a potential of 1.0 V (vs RHE) under light ON-OFF cycling. f) Comparison of the evolved oxygen gases and the charge through the external circuit of TiO_2 and ZnS_xSe_{1-x}/TiO_2 (expt.=experimental results; theor.= theoretical amount of O_2 produced, assuming a Faradic efficiency of 100%).
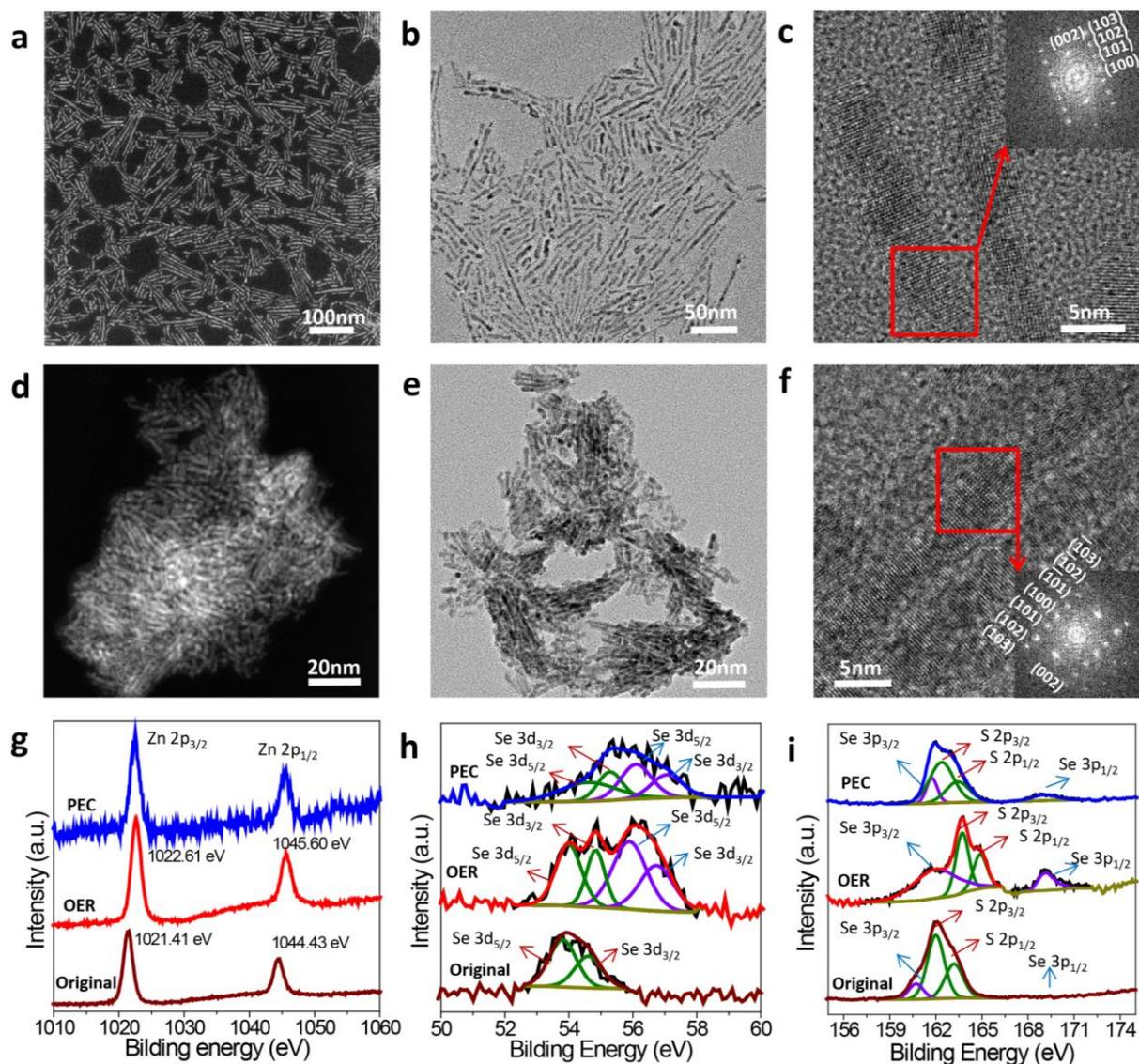
Figure 3. a-c) Electron microscopy images of alloyed $ZnS_{2/3}Se_{1/3}$ QRs after the OER test. a) HAADF-STEM. b) TEM. c) HRTEM. Inset in (c) shows FFT of selected areas of alloyed $ZnS_{2/3}Se_{1/3}$ QRs, revealing the crystallographic relations. d-f) Electron microscopy images of alloyed $ZnS_{2/3}Se_{1/3}$ QRs after the PEC test. d) HAADF-STEM. e) TEM. f) HRTEM. Inset in c,f) shows FFT of selected areas of alloyed $ZnS_{2/3}Se_{1/3}$ QRs, revealing the crystallographic relations. g-i) Comparison of XPS spectra of alloyed $ZnS_{2/3}Se_{1/3}$ QRs before and after the OER and PEC tests. g) Zn $2p$, h) Se $3d$, i) Se $3p$ and S $2p$.
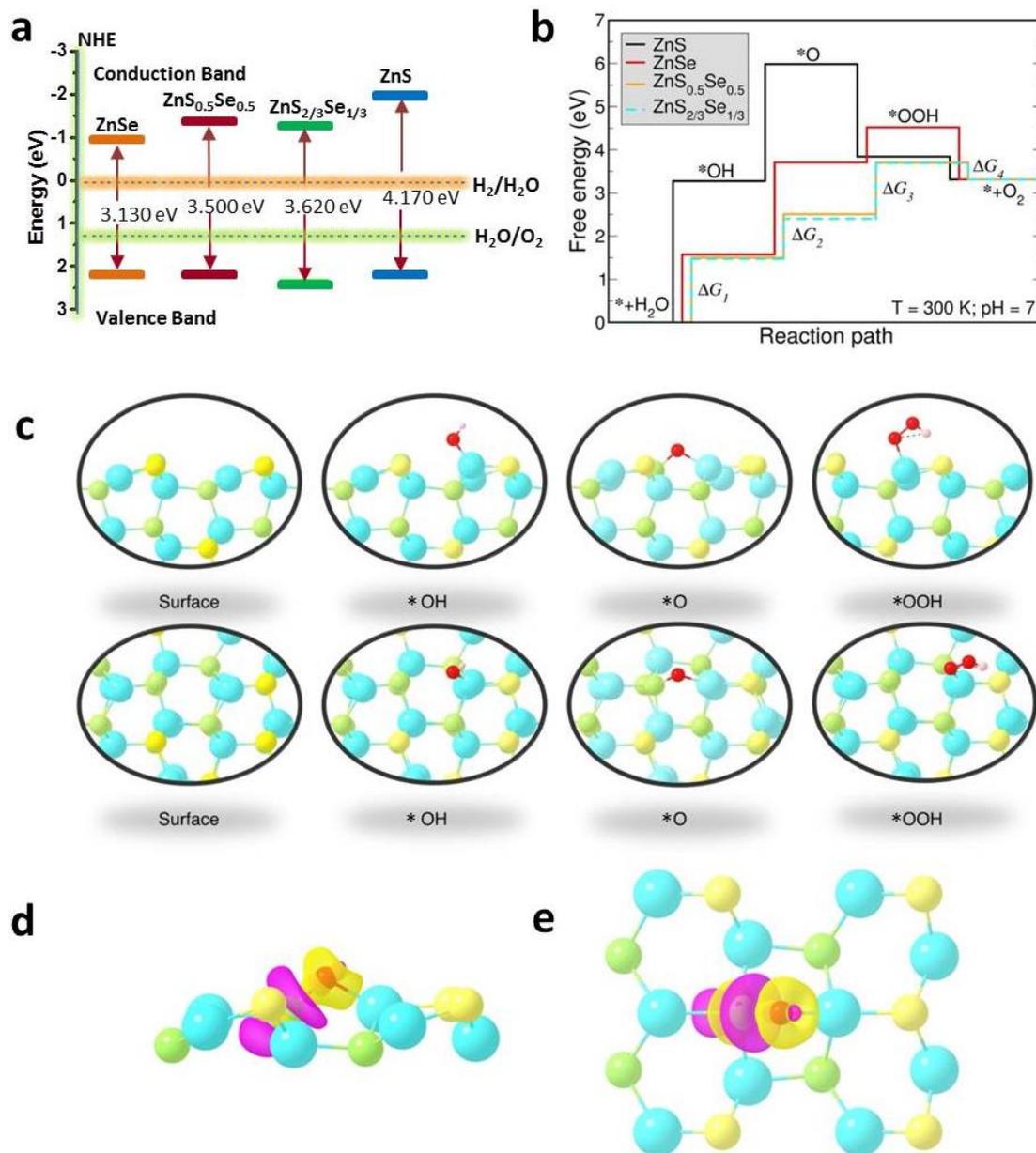
Figure 5. a) Schematic of the band gap alignment of ZnS, ZnSe and alloyed ZnS_xSe_{1-x} (x=0.5, 2/3) and the relative energies with respect to the normal hydrogen electrode level (NHE). b) Diagram of the 4-step Gibbs free energy changes calculated on (100) surface. c) Configurations of adsorbed redox species on $ZnS_{0.5}Se_{0.5}$ (100) surface associated with b). Top panel: side view; Bottom panel: top view. Colour scheme: cyan (Zn), yellow (S), green (Se), red (O), pink (H). d,e) Plot of differential charge density (magenta: charge depletion, yellow: charge accumulation) at an isosurface value of 0.004 e/Å^3 for *O species absorbed on $ZnS_{0.5}Se_{0.5}$ (100) surface. d) Side view. e) Top view.

The table of contents: Nearly monodisperse alloyed semiconductor quantum rods are formed from polydisperse nanowires by means of etching of alkylthiol. The obtained noble- and heavy-metal-free alloyed QRs demonstrate striking oxygen evolution capability and enhanced photoelectrochemical activity due to the highly active Zn sites on their (100) surface and reduced water oxidation energy barrier, as revealed by the DFT simulations.

Keyword: ZnS_xSe_{1-x}, alloyed quantum rods, noble-metal-free, heavy-metal-free, photocatalysis, oxygen evolution reaction.

Spontaneous Formation of Noble- and Heavy-Metal-Free Alloyed Semiconductor Quantum Rods for Efficient Photocatalysis

Dechao Chen, Huayang Zhang, Yunguo Li, Hongqi Sun, Lai-Chang Zhang, Shaobin Wang, Martin Saunders, Emily Barker, Guohua Jia*

ToC figure